1 **Physical mechanisms for biological carbon uptake during the onset of the spring**

2 **phytoplankton bloom in the northwestern Mediterranean Sea (BOUSSOLE site)**

3 Liliane Merlivat[1], Michael Hemming [2], Jacqueline Boutin[1], David Antoine[3, 4], Vincenzo

4 Vellucci[5], Melek Golbol[5], Gareth A. Lee[6], Laurence Beaumont[7]

5 [1] Sorbonne Université, CNRS/IRD/MNHN, LOCEAN, IPSL, Paris, France

6 [2] Coastal and Regional Oceanography Lab, Centre for Marine Science and Innovation, UNSW

7 Sydney, Sydney, NSW 2052 Australia

8 [3] Remote Sensing and Satellite Research Group, School of Earth and Planetary Sciences,

9 Curtin University, Perth, WA 6845, Australia

10 [4] Sorbonne Université, CNRS, Laboratoire d'Océanographie de Villefranche, Villefranche sur

11 Mer 06230, France

12 [5] Sorbonne Université, CNRS, Institut de la Mer de Villefranche, Villefranche sur Mer 06230,

13 France

14 [6] Centre for Ocean and Atmospheric Sciences, School of Environmental Sciences, University

15 of East Anglia, Norwich Research Park, Norwich NR4 7TJ, UK

16 [7] Division Technique INSU-CNRS, 92195 Meudon CEDEX, France

18 Correspondence to: liliane.merlivat@gmail.com

19 Keywords: Bloom onset ; Carbon uptake ; Air-sea interaction; Mediterranean sea

20 Abstract

21 Several trigger mechanisms have been proposed for the onset of the phytoplankton spring

22 bloom. Among these, that phytoplankton cells begin to bloom when they experience higher

23 average light levels in shallower mixed layers, a result of the surface net heat fluxes becoming

24 positive and wind strength decreasing. We study the impact of these two forcings in the

25 northwestern Mediterranean Sea. We take advantage of hourly measurements of oceanic and

26 atmospheric parameters collected at two neighboring moorings during the months of March

27 and April in the years 2016 to 2019, combined with glider data in 2016. We identify the onset

28 of the surface phytoplankton growth as concomitant with the start of significant biological
29 activity detected by a sudden decrease in dissolved inorganic concentrations derived from
30 measurements in the upper 10 m of the water column. A rapid reduction in wind stress
31 following high-wind events is observed at the same time. A resulting shallow mixing layer
32 favors carbon uptake by phytoplankton lasting a few days. Simultaneously, the air-sea net
33 heat flux switches from negative to positive linked to changes of the latent air-sea heat flux,
34 which is proportional to the wind speed. This results in an increased thermal stratification of
35 the ocean's surface layers. In 2016, glider data show that the mixing layer is significantly
36 shallower than the mixed layer at the onset of the surface phytoplankton bloom. We conclude
37 that decreases in the mixing and mixed layer depths lead to the onset of the phytoplankton
38 growth due to the relaxation of wind speed following storms. We estimate net daily
39 community production in the mixing layer over periods of 3 days between 2016 and 2019 as
40 between 38 mmol C m^{-2} and 191 mmol C m^{-2}. These results have important implications as
41 biological processes play a major role in the seasonal evolution of surface pCO2 and thereby
42 the rate of reduction of atmospheric CO_2 by exchange at the air-sea interface.

43

44

45

46 Introduction

47 Investigating the physical and biological mechanisms contributing to changes in air-sea
48 carbon dioxide (CO_2) fluxes is essential. It is a critical component of the global carbon cycle
49 and the climate system with the ocean removing about a quarter of the CO_2 emitted into the
50 atmosphere by human activities over the last decade. It depends on the gradient of CO_2 partial
51 pressure, pCO_2, between the atmosphere and the surface ocean [Takahashi et al., 2009;
52 Rödenbeck et al., 2013; Merlivat et al., 2015]. pCO_2 in the ocean mixed surface layer
53 depends on the relative contribution of dynamic transport, thermodynamics and
54 biogeochemistry. As the biological carbon pump lowers pCO_2 and Dissolved Inorganic
55 Carbon (DIC) at the sea surface, the production of plankton biomass during a bloom can be
56 sufficient to reverse the annual cycle of surface-ocean CO_2 uptake. A decrease in surface DIC,
57 after physical processes have been eliminated, indicates the beginning of phytoplankton
58 spring growth. Conceptual frameworks have been proposed to explain when depth-integrated

59 phytoplankton biomass starts accumulating during blooms [Behrenfeld, 2010; Sverdrup,
60 1953]. The timing of the initiation of the surface spring phytoplankton bloom depends in
61 particular on atmospheric forcing. The physical processes of wind stress, heat flux and
62 vertical mixing control the depth of the mixed/mixing layer and thus the availability of light
63 [Siegel et al, 2002, Chiswell, 2011; Taylor and Ferrari, 2011; Brody and Lozier, 2015;
64 Enriquez and Taylor, 2015, Rumyantseva et al, 2019]. Thus, to better understand which
65 fundamental physical processes control the timing of the onset of the surface bloom, in situ
66 measurements are needed at the appropriate hourly to daily timescale. It is important to draw
67 attention to the atmospheric forcing timescale. In biogeochemical ocean modeling studies,
68 typically built on atmospheric models, reanalysis or satellite data, time resolution of at best a
69 few days are required [Mahadevan et al, 2012].
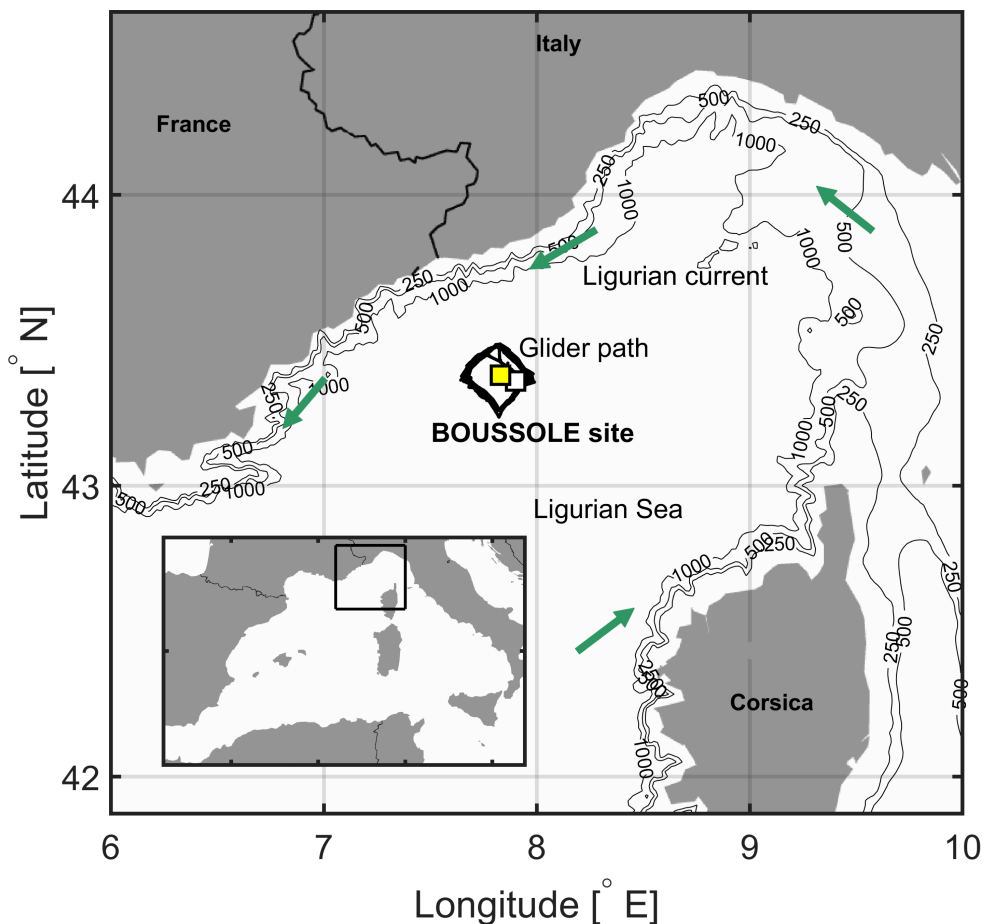
70

71 Figure 1. The area of the northwestern Mediterranean Sea showing the French and Italian
72 Rivieras, the island of Corsica, the main current branches (green arrows) in the Ligurian Sea
73 and the location of the BOUSSOLE buoy (white square) and the AZUR meteorological buoy
74 (yellow square). The black line indicates the glider's path in March-April 2016.

75 In the northwestern Mediterranean Sea, the BOUSSOLE (Bouée pour l'acquisition de Séries
76 Optiques à Long Terme; Antoine et al., 2006, 2008a,b) buoy is located in the central area of
77 the Liguro-Provençal basin (Fig.1), where the dominant ocean currents are generally weak
78 (<20 cm s^{-1}) [Millot, 1999; Antoine et al., 2008b; Niewiadomska et al., 2008]. The main
79 processes that govern the pCO$_2$ variations at the sea surface on an annual scale, after removal
80 of the temperature effect, are vertical convective mixing and biological production [Begovic
81 and Copin-Montégut, 2002; Copin-Montégut al., 2004; Hood and Merlivat, 2001; Merlivat et
82 al., 2018]. Intense convection resulting from repeated high wind events in winter or early
83 spring when atmospheric temperatures are typically low brings nutrients to the surface layer
84 [Andersen and Prieur, 2000; Antoine et al., 2008b; Marty et al., 2002; Pasqueron de
85 Fommervault et al., 2015].

86 The objective of this study is to examine the impact of atmospheric forcing on surface
87 phytoplankton bloom initiation in the northwestern Mediterranean Sea. To this aim we use
88 concurrent hourly data of seawater carbon chemistry measured at depths less or equal to 10 m
89 at the BOUSSOLE mooring [Merlivat et al, 2018] and atmospheric flux measurements at the
90 Azur meteorological buoy 3.1 nm (5.8 km) away from BOUSSOLE in March and April 2016
91 to 2019. Additional measurements of phytoplankton chlorophyll-a (Chla), temperature and
92 density were provided by an underwater glider deployed in March-April 2016. The initiation
93 of biological carbon uptake is revealed by the sudden decrease in DIC measured at the
94 BOUSSOLE buoy.

95 In the Material and Methods section, we provide the description of data processing,
96 theoretical framework, and calculations used to evaluate mixing regimes in the water column
97 and net community production. The results section presents measured atmospheric and
98 biogeochemical parameters observed in March-April, and NCP estimates from 2016 to 2019.
99 The Discussion section relates our results to previous findings and presents our conclusions
100 regarding the drivers of phytoplankton bloom initiation.

101

102 2 Material and methods

103 2.1- Data from the BOUSSOLE mooring

104 CARIOCA sensors [Merlivat and Brault, 1995] installed on the BOUSSOLE buoy (43°22'N,
105 7°54'E; Fig.1) monitored hourly partial pressure, pCO$_2$, at both 3 and 10 m alongside salinity

106 and temperature (SEABIRD Scientific SBE 37 MicroCAT CTDs). Protocols for calibration of

107 in situ measurements are described in [Merlivat et al, 2018]. CARIOCA measurements of

108 pCO_2 and temperature are combined with total alkalinity (Alk) derived from salinity

109 [Merlivat et al., 2018] to calculate DIC. The dissociation constants of Mehrbach et al., (1973)

110 refitted by Dickson and Millero (1987) are used, as recommended by Alvarez et al. (2014) for

111 the Mediterranean Sea. For the March-April months mean salinity is 38.3, corresponding with

112 mean Alk equal to 2571.4 µmol kg^{-1} [Copin et al, 2004]. The expected precision of the

113 CARIOCA pCO_2, and DIC is 5 µatm, and 3 µmol kg^{-1}, respectively [Merlivat et al, 2018].

114 2.2- Glider observations

115 An iRobot Seaglider model 1KA (SG537) with an ogive fairing operated by the University of

116 East Anglia (UEA) [see Hemming et al., 2017] was deployed during the BOUSSOLE

117 monthly cruise (#169) [Golbol et al 2000] and recovered 1 month later with a ship of

118 opportunity. Diving to 1000 m, 147 dives were completed between March 7 and April 5 2016

119 repeatedly-sampling a square-shaped path surrounding the BOUSSOLE buoy (Fig. 1) with

120 corners pointing to cardinal directions. Out of 147 dives, a number of them contain data that

121 are within 10 km of the BOUSSOLE mooring, i.e. when it was sampling in the eastern corner

122 of the diamond path. The glider was equipped with a non-pumped SEABIRD Scientific SBE

123 9 CTD instrument package providing temperature and salinity, and a WET Labs Eco Puck

124 sensor providing relative phytoplankton Chla fluorescence, factory calibrated into Chla

125 concentration units (mg m^{-3}) locally adjusted with top 10 m HPLC chlorophyll from CTD

126 and mooring samples.

127

128 2.3- Azur meteorological buoy

129 The Azur meteorological buoy has been deployed since 1999 by the French weather forecast

130 Agency (Meteo-France) at 43°23'N, 7°50'E (Fig. 1). It provides hourly measurements of

131 surface wind speed extrapolated to 10 m height, U_{10} (m s^{-1}), net incoming and emitted long-

132 wave radiation, incoming short-wave radiation, and the sensible and latent heat fluxes. These

133 are needed to estimate the net air-sea heat budget at the sea surface (http://mistrals.sedoo.fr).

134 U_{10} is used to calculate wind stress, τ, as follows: $\tau = \rho_a \, C_d \, U_{10}^{2}$, where ρ_a is air density (1.2

135 kg m^{-3}), and C_d is the drag coefficient (1.4 x 10^{-3}). Photosynthetically Active Radiation (PAR,

136 mol photons m-^{2} d^{-1}) is related to solar irradiance (i.e. short-wave flux), SW, following PAR =

137 0.473 SW [Papaioannou et al., 1993].

138   2.4- Estimation of mixed and mixing layer depths

139   The mixing layer depth, Z_{mx}, is the upper part of a mixed layer of uniform density where

140   active turbulence occurs [Brainerd and Gregg 1995]. Several recent studies have highlighted

141   the significance of this layer to understand the phytoplankton phenology of phytoplankton

142   blooms [Brody and Lozier, 2015; Taylor and Ferrari, 2011]. Autonomous profiling floats

143   equipped with bio-optical sensors have also highlighted the importance of mixing rather than

144   mixed layers to characterize the onset and the development of a phytoplankton bloom. Wind-

145   driven and buoyancy-driven regimes control the characteristics and depth of active mixing

146   [Brody and Lozier, 2014, 2015, Ramuyantseva et al, 2015, Lacour et al, 2019, Pellichero et al,

147   2020]. Wind-driven mixing dominates in the presence of weak buoyancy forcing when heat

148   fluxes are small. In that case, the dominant mixing length scale is equal to the Ekman length

149   layer depth scale.

150   The daily mean mixed layer depth, Z_{ml} is derived for 2016 from glider vertical profiles of

151   temperature and salinity using the algorithm provided by Holte and Talley, (2009) estimated

152   using the potential density algorithm.

153   To estimate Z_{mx}, τ is used to calculate the Ekman layer depth, Z_{ek}, $Z_{ek} = \gamma\, u_* / f$, where γ is an

154   empirical constant (0.5), f is the Coriolis parameter (10^{-4} s^{-1}) over the BOUSSOLE area, and

155   u_* is the turbulent friction velocity, $u_* = \sqrt{\dfrac{\tau}{\rho_w}}$ (m s^{-1}), with ρ_w the density of the surface sea

156   water [Lacour et al, 2019]. When heat fluxes are large and positive, Enrikez and Taylor

157   (2015) proposed to express the mixing depth Z_{mx} in terms of the surface forcing, i.e. the

158   surface stress and a stabilizing surface buoyancy flux B_0, as follows:

159
$$\frac{1}{Z_{mx}^2} = \frac{f^2}{(C_3\, u_*)^2} + \frac{f\, B_0}{(C_4\, u_*^2)^2} \qquad (1)$$

160   With $C_3 = 1$, $C_4 = 0.57$, $B_0 = Q\, \lambda\, g\, / c_p\, \rho_0$, where Q is the net surface heat flux, λ the thermal

161   expansion coefficient (1.65 10^{-4} $°C^{-1}$), g the gravitational acceleration (9.81 m s^{-2}) c_p the

162   specific heat of water (4 10^{-3}J kg^{-1} $°C^{-1}$) and ρ_0 the pure water density (1000 kg m $^{-3}$).

163   2.5-Estimation of euphotic zone depth

164   The euphotic depth, Z_{eu}, is generally derived as the depth where PAR is 1% of its surface

165   value. Z_{eu} can be estimated from Chla at the surface using the method described by Lee et al.

166   (2007) based on the equation of Morel and Berthon (1989):

$$Z_{eu} = 34 \, (Chla)^{-0.39} \quad (2)$$

For the period between 2017 and 2019, GlobColour merged Chla products were used, which are based on satellite observations with a resolution of 25 km, and a binning period of 8 days (http://www.oceancolour.org). For 2016, glider surface Chla was used to derive Zeu instead of satellite measurements. We excluded glider Chla between 05:00 and 20:00 UTC affected by sunlight–induced fluorescence quenching, and we applied a depth-constant offset to glider measurements using Chla water samples available on March 7.

2.6-Estimation of average mixing layer irradiance

We calculate the average mixing layer irradiance, I, function of the incident surface irradiance, PAR, mixing layer depth, h, and the diffuse attenuation coefficient, K_d, estimated from surface chlorophyll-a concentrations (Venables and Moore, 2010).

$$K_d = 0.05 + 0.057 \, Chla^{0.58}$$

$$I = \frac{PAR}{K_d h} \left(1 - e^{-K_d h}\right) \quad (3)$$

2.7 – Estimation of net community production

Biological Net Community Production rates, NCP (mmol m^{-2} day^{-1}), are calculated for separate 3-day periods in March-April, 2016 to 2019 from DIC concentrations derived from CARIOCA measurements, assuming that measurements in the top 10 m of the water column are representative of an homogeneous mixing layer [Boutin and Merlivat, 2009; Merlivat et al, 2015; Pelicherro et al, 2020]. In the study area, current velocities are expected to be small [Millot, 1999; Antoine et al., 2008; Niewiadomska et al., 2008], hence to estimate NCP, we assume that the contribution of horizontal advection was negligible. Vertical mixing events are identified by an increase in DIC resulting from upward movement of high DIC Levantine Intermediate Water (LIW) at approximately 200 m depth [Copin-Montégut and Bégovic, 2002]. We isolated time periods when local physical processes were largely one-dimensional in order to study changes in biological and chemical parameters that occurred during rapid transitions from deep mixing to intermittent stratification. In 2016, over a four-day period, March 18-21, the diurnal cycle of DIC values characterized by a maximum in the morning followed by a minimum at the end of the day indicates the onset of organic matter formation. The eddy diffusion term is negligible as the DIC gradient at the base of the mixing layer is

196 very weak, entrainment is not expected as changes in DIC are observed during periods of
197 stratification. For the identified periods, biological production and air-sea exchange are the
198 dominant processes responsible for daily changes in DIC.

199 NCP is thus estimated from temporal variation of the DIC integrated over Z_{mx} (DIC_{int}), and
200 corrected for the air-sea CO_2 flux contribution [Pelicherro et al, 2020]:

201 $$NCP = \left(\frac{\Delta DIC_{int}}{\Delta t}\right)_{bio} = \left(\frac{\Delta DIC_{int}}{\Delta t}\right)_{meas} - k \times s \times (pCO_{2atm} - pCO_{2sw}) \quad (4)$$

202 The first term in equation 4, $\left(\frac{\Delta DIC_{int}}{\Delta t}\right)_{meas}$, is the daily variation of DIC_{int} calculated over 3
203 days from the date identified as the start of phytoplankton growth (t_0), whilst the remaining
204 part corresponds to DIC variability due to air-sea CO_2 exchange, where k is the gas transfer
205 velocity [Wanninkhof, 2014], s is the solubility of CO_2 in seawater [Weiss, 1974], and
206 pCO_{2sw} and pCO_{2atm} are respectively the partial pressures of CO_2, in µatm, in sea water and in
207 air [Merlivat et al, 2018].

208 3 Results

209 3.1- Description of the 2016 time-series
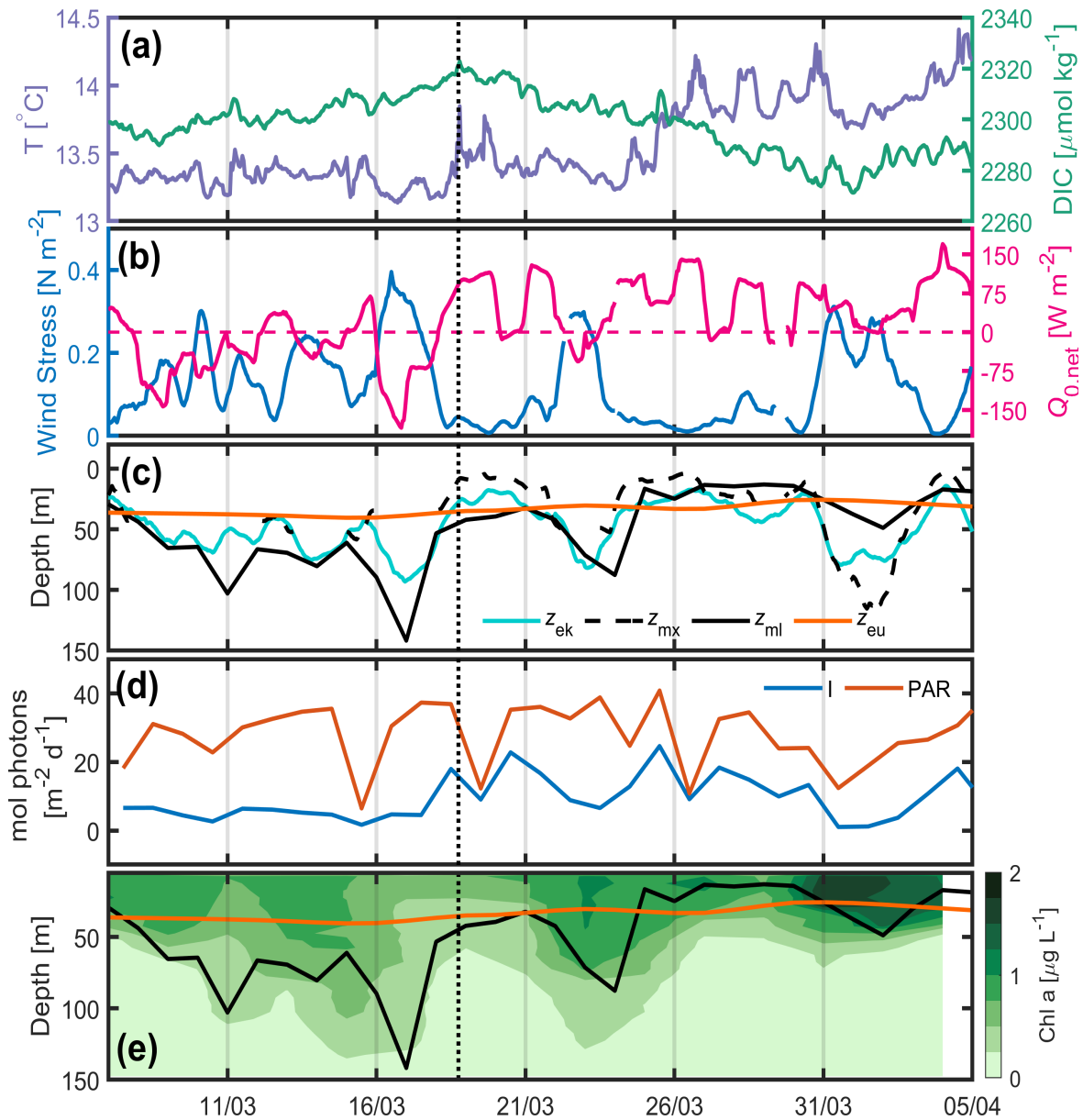
210

Figure 2. 2016 (a) Hourly DIC (green) and SST(purple) at the BOUSSOLE site, (b) hourly wind stress (blue) and net heat flux (pink) at the Azur buoy site. The pink dotted line indicates the change of sign of the net heat flux from negative to positive values, (c) daily depths of the mixed layer (black), mixing layer (dotted black), Ekman layer (cyan) and euphotic layer (orange) at the BOUSSOLE site. The black dotted line on panels (a), (b), (c) (d) and (e) indicates the beginning of DIC decrease on March 18. (d) PAR (orange) and I, average mixing layer irradiance (blue), (e) Glider-derived depths of the mixed layer (black curve, same as in (c)), euphotic layer (orange), and nighttime 2-day binned chlorophyll concentration (green coloring) retrieved between March 7 and April 5.

220   Physical and biogeochemical parameters have been measured between March 7 and April 5
221   2016 (Fig. 2). We observe an initial increase in DIC until March 18 (Fig. 2a), resulting from
222   the vertical mixing of surface waters with the DIC-enriched underlying LIW [Copin-
223   Montégut and Bégovic, 2002], followed by a decrease in DIC that corresponds to an increase
224   of surface Chla (Fig 2e). Temperature increases intermittently over the same time period (Fig.
225   2a), with a sharp increase on March 18 and 25. Before March 18 frequent atmospheric fronts
226   associated with wind forcing between 0.2 and 0.5 N m^{-2} were observed (Fig. 2b). $Q_{0,net}$ was
227   negative most of the time leading up to March 18, but mostly positive afterwards (Fig. 2b). A
228   clear anticorrelation was observed between τ and $Q_{0,net}$ (Fig. 2b). The mixed-layer depth
229   derived from the glider measurements (< 20 km away from the Boussole site) deepened to >
230   70 m at times between March 8 and March 18, consistent with the passage of frequent
231   atmospheric fronts. From March 18 to April 5, Z_{ml} shoaled from ~ 45 m to ~10 m, excluding
232   two short periods around March 24 and April 2 when atmospheric fronts were passing (Fig.
233   2c). From March 18 to 31, Z_{mx} was for a considerable time either shallower than, or at similar
234   depth to Z_{ml} and Z_{eu} (Fig. 2c). The start of the increase in PAR from March 15 precedes the
235   increase in irradiance by 3 days as a result of the decrease of the mixing layer depth observed
236   only after March 18 (Fig. 2d).

237   During periods of a few days, from March 7 to April 5, increases in glider Chla were
238   observed as the result of a series of net accumulation/mixing events. Following the initial
239   growth of surface phytoplankton identified by the DIC decrease on March 18, biomass
240   accumulation was observed a few days later (Fig. 2e) .The same was observed in the Southern
241   Ocean [Pelicherro et al, 2019].

242   3.2- Description of the 2017-2018-2019 time-series

243   Only measurements at the BOUSSOLE and Azur buoys were available between 2017 and
244   2019. Here we focus on the periods between March 1 and April 25. In 2017, from March 9,
245   after the passage of a very active atmospheric front (τ up to 2.7 N m^{-2}), a decrease in DIC
246   accompanied by an increase in temperature was observed for a period of 14 days despite a
247   few short bursts of vertical mixing, typically lasting less than 1 day (Fig.3a, d, g). At the same
248   time, the net surface heat flux switched from negative to positive most of the time. Over this
249   14-day period, Z_{mx} was predominantly shallower than the Z_{eu} at times when DIC was
250   decreasing.

In 2018 (Fig. 3b, e, h) and 2019 (Fig. 3c, f, i), the weather records throughout the month of March are very similar, showing a succession of very strong wind events at the start of the investigated time periods, with τ values of up to 3.7 N m^{-2} and Z_{ek} values as deep as 300 m. On April 5, 2018, following a period of high wind stress resulting in the formation of a deep mixing layer (~250 m), a decrease in DIC and an increase in SST were observed over 3 days. At the same time, the net heat flux oscillated around zero. In 2019, CARIOCA data were only available after March 24. On March 30, 3 days after high winds, a decrease in DIC and an increase in temperature lasted 3 days, while simultaneously the net heat flux reversed from negative to positive.
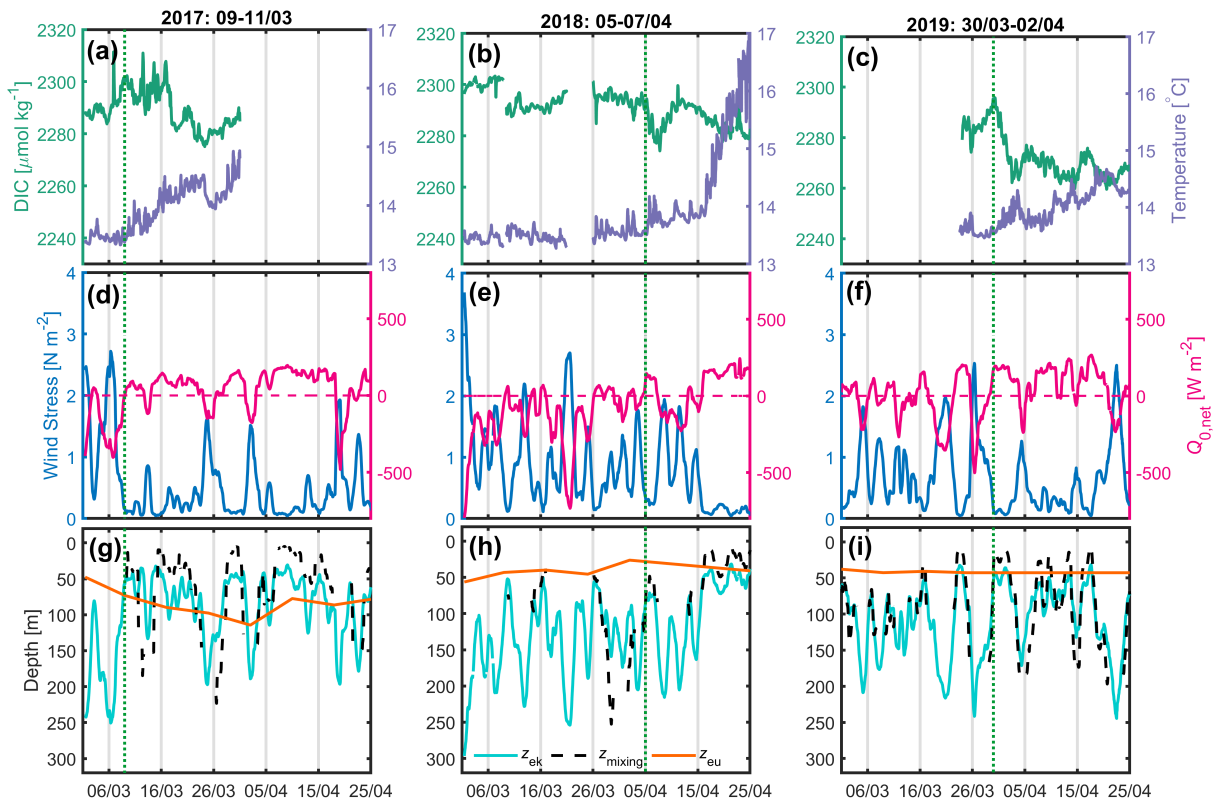
Figure 3. (a, b, c) 2017, 2018 and 2019 DIC (green) and SST (purple) at the BOUSSOLE site, (d, e, f) wind stress (blue) and net heat flux (red) at the Azur buoy site. (d, e, f) The red dotted line indicates the change of sign of the net heat flux from negative to positive values, (g, h, i) depths of the mixing layer (dotted black), Ekman layer (cyan) and euphotic layer (orange) at the BOUSSOLE site. The vertical dotted green line indicates the onset of the decrease of DIC.

For the period between 2017 and 2019, only satellite chlorophyll-a concentrations with a binning period of 8 days were available, which is too large to calculate the average mixing irradiance as it is highly variable on a daily scale (Fig 2.d).

3.3- NCP

NCP was estimated (Eq. 3) for 3-day periods over the four time-series between 2016 and 2019 (Table 1). Because we compute NCP only during periods when Z_{ml} and Z_{mx} shoal and the air-sea CO_2 flux is very small, the measured total daily changes of DIC, dDIC/dt (correlation coefficient, $r^{*2} > 0.70$), is expected to represent the biological consumption of DIC. In 2016, 2017, and 2019, daily biological carbon uptake fluxes are between 38 and 191 mmol m^{-2} d^{-1}. PAR and I vary respectively from 30 to 53 and 13 to 25 mol photons m^{-2} d^{-1} for the four considered periods (Table 2).

	T_0	dDIC/dt [a]	r^{*2} [b]	ΔDIC / Δt [c]	r^{*2} [d]	air-sea flux CO_2 [e]	NCP [f]
		µmol kg^{-1}d^{-1}		mmol m^{-2}d^{-1}		mmol m^{-2}d^{-1}	mmol m^{-2} d^{-1}
2016 10m	March 18	-3.0	0.80	-37	0.68	1	38
2017 3m	March 9	-4.5	0.84	-188	0.86	3	191
2018 3m	April 5	-6.5	0.70			17	
2019 10m	March 30	-8.3	0.93	-163	0.63	4	167

Table 1. Net community production computed in the mixing layer over 3 days (NCP) after the bloom onset (T_0). (a, b) variation of DIC at the measurement depth and linked correlation coefficient; (c, d) change of integrated DIC over Z_{mx} and linked correlation coefficient ;(e) CO_2 flux from the atmosphere to the ocean; (f), absolute value of calculated NCP is considered in order to provide positive values throughout the presentation and discussion in the manuscript.

4 Discussion

287   4.1 Analysis of the physical drivers of the bloom initiation over the 4 years, 2016-2019

288   4.1.1 In 2016, the consumption of carbon indicated by the decrease in DIC from March 18
289   attests the initiation of the formation of phytoplankton biomass (Fig. 2,). Between 2
290   successive days, March 17 and 18, a rapid decrease in daily wind stress from 0.24 to 0.04 N
291   m^{-2} results in a change of sign of the net heat flux from -68 to +56 W m^{-2} (Fig.4a) and a
292   shoaling Z_{mx}, which is for the most part shallower than Z_{eu} (Fig.4b) after March 18.
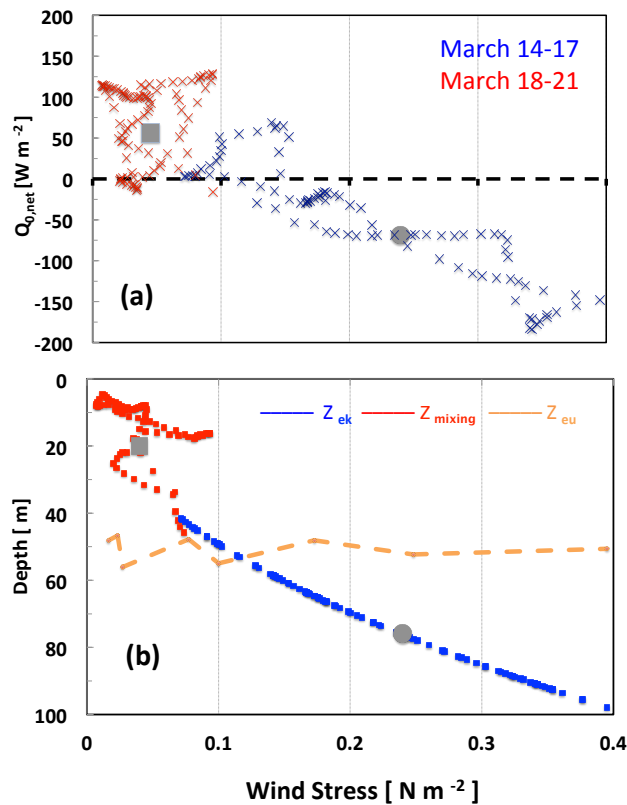
293

294   Figure 4. Changes of physical parameters (hourly values) at the onset of the 2016 bloom
295   during 2 consecutive periods of 4 days, March 14-17 (blue) and March 18-21 (red) as a
296   function of wind stress (a) net surface heat flux (b) depths of the Ekman, mixing and euphotic
297   layer. Grey circles and grey squares indicate mean values respectively on March 17 and
298   March 18. For comparison, the orange line shows the euphotic layer depth (March 14-21).

299   This illustrates the very fast change in heat flux and mixing layer thickness resulting from the
300   decrease in wind stress. The main drivers to explain the initiation of near surface spring
301   phytoplankton blooms proposed by [Taylor and Ferrari, 2011, Brody-Lozier, 2014, 2015] are
302   a decrease in wind strength, a positive surface heat flux, and a decrease in the dominant

303   mixing length scale. Our results indicate that a decrease in τ is a common component for these

304   last two mechanisms (Fig.4). The variability of $Q_{0,net}$ is strongly controlled by the variability

305   of the latent heat flux proportional to the wind speed. From March 17 to 18, the latent heat

306   flux changed by 84 W m^{-2} representing nearly 2 thirds of the total change of Q_0, with the

307   remainder originating from an increased short-wave flux. Hence, $Q_{0,net}$ increased as τ

308   decreased. In the same way Z_{mx}, which is related to τ and $Q_{0,net}$, decreased. This highlights the

309   major contribution of wind stress relaxation in controlling the net surface heat flux, and

310   subsequent stratification leading to sallower Z_{mx}

311   4.1.2 Over the 4 years, 2016-2019, during the months of March and April, at the very

312   beginning of spring, the conditions required for initiating the spring bloom are very similar

313   although the range of wind stress values is smaller in 2016 (Fig. 2, Fig. 3). The wind stress

314   values are low following storm events. For all years except 2018, Z_{mx} is smaller than Z_{eu}. The

315   average atmospheric and oceanographic conditions during the onset of the bloom are shown

316   in Table 2. The decrease of wind-driven mixing is then a dominant physical mechanism,

317   namely mixed layer shoaling which best predicts the timing of the spring bloom [Brody

318   Lozier, 2014, 2015]. Likewise, in the Southern Ocean, Pelicherro et al (2020) showed that a

319   bloom is initiated only when the wind-driven mixed layer decreases, even if the net heat flux

320   has been positive for some months.

321   4.2 DIC, Chla, Irradiance at the ocean surface in 2016

322   Between March 18 and 21, a diurnal cycle in DIC is observed (Figure 5a) characterized by a

323   maximum in the morning followed by a minimum at the end of the day, indicating the onset

324   of organic matter formation. The decrease in DIC is accompanied by an increase of glider

325   surface Chla on March 18 and a simultaneous increase in the average mixing layer irradiance

326   (Fig. 5 b). It is worth noting that the Chla maximum does not occur until 31 March, 13 days

327   after the first decrease in DIC. This maximum is the one identified in most cases by the Chla

328   satellite measurements with a binning period of 8 days. It follows that satellite data cannot

329   accurately characterize the conditions that prevail for the onset of the phytoplankton

330   growth, as these are dictated by a great temporal variability of atmospheric forcings.

331   Due to the seasonal increase of surface irradiance, as well as the availability of nutrients

332   following vertical mixing with intermediate nutrient-enriched waters [Begovic and Copin-

333   Montégut, 2002], the conditions for the onset of a bloom are met.

334
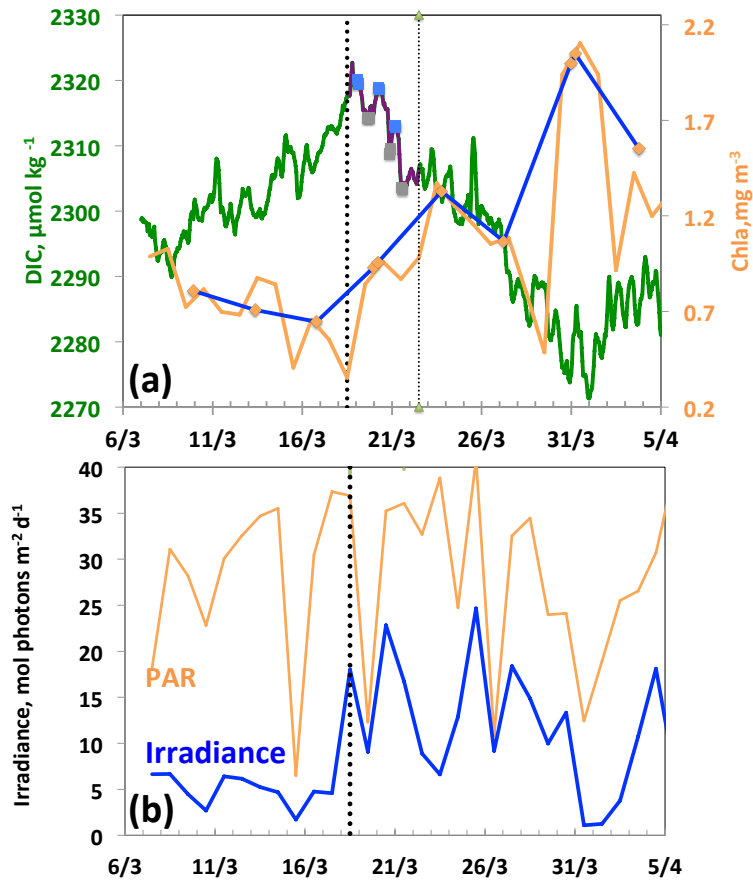
335

Figure 5. From March 7 to April 5, (a) DIC and Chla. The purple line and the squares (blue,morning; grey, evening) indicate the 3 days biological diurnal DIC changes during the period considered to compute NCP The blue and orange lines indicate the surface Chla when the glider was at a distance of less than 5 km (blue) and less than 20 km (orange) respectively from the Boussole buoy. (b) PAR and I average mixing layer irradiance. The vertical dotted black line indicates the onset of the bloom on March 18.

4.3- Biological carbon uptake

In 2016, 2017, and 2019, at the onset of the bloom Z_{mx} is shallower than Z_{eu} (Table 2). Two factors account for the observed large range of NCP variability at the time of triggering the bloom: dDIC/dt and Z_{ml}. In 2016 and 2017, DIC decreased over a period of 14 days, whereas it lasted for 3 days in 2018 and 2019, as a result of short-lived high wind events ($\tau > 1$ N m^{-2}). On April 2, 2018, a high surface phytoplankton Chla, 1.9 mg m^{-3}, was measured by satellite (Globcolour data) suggesting a strong biological signal. However, as Z_{eu} is significantly shallower than Z_{mx} (26 m vs. 65m; Fig. 3h), it would be incorrect to estimate NCP integrated

over Z_{mx} using the DIC gradient measured at 3 m depth and likewise to compute the average mixing layer irradiance.

At the nearby DyFAMed site (Dynamique des Flux Atmospheriques en Mediterranee), using a 20-year O_2 time series, Coppola et al. (2018) estimated an annual net community carbon production equal to 7.1 mol m^{-2} yr^{-1}, or 19.4 mmol m^{-2} d^{-1}. Additionally, using determinations of primary production from ^{14}C in-situ incubations and of carbon export fluxes from sediment traps at DyFAMed, Marty and Chiaverini (2002) calculated average daily primary productions between 19.6 and 53 mmol m^{-2} d^{-1}. These estimates may have underestimated the annual NCP values as they were calculated from monthly observations while phytoplankton production varies on a daily timescale. Our DIC measurements highlight the large short-term variability of carbon consumption over a few days in March-April when bloom-triggering atmospheric conditions are met, such as a seasonal light increase and the availability of nutrients.

	T_0	Wind stress	Net heat flux	PAR	Z_{mixing}	$Z_{Euphotic}$	Irradiance
		N m^{-2}	W m^{-2}	mol photons m^{-2}d^{-1}	m	m	mol photons m^{-2}d^{-1}
2016	March 18	0.04 +/0.02	56+/-36	37+/-3	20+/-9	47	18
2017	March 9	0.12+/-0.02	45+/-21	30+/-3	28+/-12	71	13
2018	April 5	0.30+/-0.24	127+/-12	42+/-6	62+/-9	29	
2019	March 30	0.10+/-0.02	183+/-9	53+/-2	20+/-5	43	25

Table 2.   2016-2019.   Atmospheric drivers of the onset of the bloom: average values and standard deviation on the day of the start of the bloom, T_0.

5- Concluding remarks

Around March and April in the northwestern Mediterranean Sea, the seasonal change in lighting conditions and atmospheric forcing are the essential parameters that control the triggering of near-surface phytoplankton blooms. These mechanisms have been highlighted through the coupling of high-frequency physical and biogeochemical in situ observations. For years 2016 to 2019, a bloom started in March or early April identified by a decrease in surface

DIC, following a period of intense mixing. The rapid decrease in surface wind speed entailed a switch from negative to positive air-sea net heat fluxes, essentially due to changes in the latent air-sea heat flux proportional to wind speed. These analysis support the hypothesis that decreases in the depth of active mixing, a result of the transition from buoyancy-driven to wind-driven mixing, control the timing of the surface spring bloom.

We have shown that the onset of surface phytoplankton growth, identified in 2016 by a simultaneous initial decrease in DIC and an increase in surface Chla, precedes by a few days the surface chlorophyll maximum when detected by satellite measurements with a binning period of 8 days. This time span does not allow to identify precisely the contribution of atmospheric drivers to trigger the onset of the growth of phytoplankton as it occurs on a daily basis.

Data availability

BOUSSOLE data (2016-2019) are available in the SEANOE data base (Merlivat Liliane, Boutin Jacqueline (2020). Mediterranean Sea surface CO_2 partial pressure and temperature data. SEANOE. https://doi.org/10.17882/56709

Azur Meteorological buoy: http://mistrals.sedoo.fr

SChl, 8-day, 4 km x4 km resolution, level 3 mapped ocean color product distributed by the European Space Agency, available at http://www.ocean colour/org

All glider data is archived at the British Oceanographic Data Centre (BODC, https://www.bodc.ac.uk/data/bodc_database/gliders/).

Author contributions: VV and MG were respectively in charge of the BOUSSOLE mooring buoy maintenance and monthly water sampling. LB was responsible for the laboratory preparation and calibration of the CARIOCA sensors. GAL led the UEA glider mission in March-April 2016. DA and VV provided data and funding through the BOUSSOLE project and contributed to writing and editing of the manuscript.

The authors declare that they have no conflict of interest.

402 Acknowledgments: Michael Hemming was a PhD student at the University of East Anglia
403 and Sorbonne University under the supervision of Prof. Jan Kaiser, Prof. Karen J. Heywood,
404 Dr Dorothee Bakker and Dr Jacqueline Boutin, funded by the Defence, Science and
405 Technology Laboratory (Contract no. DSTLX1000092277) with cooperation with Direction
406 Générale de l'Armement (DGA)-. The assistance of the UEA Glider Group in keeping the
407 glider flying is also gratefully acknowledged. The BOUSSOLE time series project is funded
408 by the Centre National d'Etudes Spatiales (CNES) and the European Space Agency
409 (ESA/ESRIN contract 4000119096/17/I-BG). The authors acknowledge Météo-France for
410 supplying the data from the Azur buoy and the HyMeX database teams (ESPRI/IPSL and
411 SEDOO/Observatoire Midi-Pyrénées) for their help in accessing their data. Crew and
412 Captains of R/V Tethys II are warmly thanked for assistance with operations at sea.

413 We thank two reviewers for their careful and conscientious reviews.

414

415 References

416 Álvarez, M., Sanleón-Bartolomé, H., Tanhua, T., Mintrop, L.,Luchetta, A., Cantoni, C.,
417 Schroeder, K., and Civitarese, G.: The CO2 system in the Mediterranean Sea: a basin wide
418 perspective, Ocean Sci., 10, 69–92, https://doi.org/10.5194/os-10-69-2014,2014.

419 Andersen, V. and Prieur, L.: One-month study in the open NW Mediterranean Sea
420 (DYNAPROC experiment, May 1995): Overview of hydrobiogeochemical structures and
421 effects of wind events, Deep-Sea Res. I, 47, 397–422, 2000.

422 Antoine, D. M. Chami, H. Claustre, F. D'Ortenzio, A. Morel, G. Bécu, B. Gentili, F. Louis ,J.
423 Ras, E. Roussier, A.J. Scott, D. Tailliez, S. B. Hooker, P. Guevel, J.-F. Desté, C. Dempsey
424 and D. Adams. 2006, BOUSSOLE : a joint CNRS-INSU, ESA, CNES and NASA Ocean
425 Color Calibration and Validation Activity. NASA Technical memorandum, N° TM-2006-
426 214147, NASA/GSFC, Greenbelt, USA.

427 Antoine, D., P. Guevel, J.-F. Desté, G. Bécu, F. Louis, A.J. Scott and P. Bardey: The
428 «BOUSSOLE» buoy; a new transparent-to-swell taut mooring dedicated to marine optics:
429 design, tests and performance at sea, Journal of Atmospheric and Oceanic Technology, 25,
430 968-989, 2008a.

431 Antoine, D., F. d'Ortenzio, S. B. Hooker, G. Bécu, B. Gentili, D. Tailliez, and A. J. Scott:
432 Assessment of uncertainty in the ocean reflectance determined by three satellite ocean color
433 sensors (MERIS, SeaWiFS and MODIS-A) at an offshore site in the Mediterranean Sea
434 (BOUSSOLE project), Journal of Geophysical Research, 113(C7), 2008b.

435 Begovic , M., and C. Copin-Montegut, Processes controlling annual variations in the partial
436 pressure of fCO_2 in surface waters of the central northwestern Mediterranean sea (Dyfamed
437 site), Deep-Sea Research II, 49, 2031-2047, 2002

438 Behrenfeld, M. J, Abandoning Sverdrup's critical depth hypothesis on phytoplankton blooms.
439 Ecology, 91(4), 977-989, 2010

440 Behrenfeld, M. and E. Boss, Resurrecting the ecological underpinnings of ocean plankton
441 blooms. Annual Review of Marine Science, 6, 167-194, DOI: 10.1146/annurev-marine-
442 052913-021325, 2014

443 Brainerd, K. E., and Gregg, M. C, Surface mixed and mixing layer depths. Deep Sea Research
444 I: Oceanographic Research Papers, 42:1521–1543, 1995

445 Brody, S., and Lozier,M. Changes in dominant mixing length scale as a driver of
446 phytoplankton bloom initiation in the North Atlantic, Geophysical Research Letters 41, 3197–
447 3206, 2014.

448 Brody, S. R., & Lozier, M. S. , Characterizing upper-ocean mixing and its effect on the spring
449 phytoplankton bloom with in situ data. ICES Journal of Marine Science, 72(6), 1961-1970,
450 2015.

451 Chiswell, S. M.: Annual cycles and spring blooms in phytoplankton: don't abandon Sverdrup
452 completely. Marine Ecology Progress Series, 443, 39-50, 2011.

453 Copin-Montégut, C., Begovic, M.: Distributions of carbonate properties and oxygen along the
454 water column (0– 2000 m) in the central part of the NW Mediterranean Sea (Dyfamed site).
455 Influence of winter vertical mixing on air– sea CO_2 and O_2 exchanges. Deep-Sea Res., Part 2,
456 Top. Stud. Oceanogr. 49, 2049– 2066, 2002.

457 Copin-Montégut, C., M. Bégovic, and L. Merlivat.: Variability of the partial pressure of CO_2
458 on diel to annual time scales in the Northwestern Mediterranean Sea, Mar Chem, 85(3-4),
459 169-189, 2004.

460   Coppola, L., Legendre, L., Lefevre, D., Prieur, L., Taillandier, V., & Riquier, E. D. :

461   Seasonal and inter–annual variations of dissolved oxygen in the northwestern Mediterranean

462   Sea (DYFAMED site). Progress in Oceanography, 2018.

463   Dickson, A. G., and F. J. Millero .: A comparison of the equilibrium constants for the

464   dissociation of carbonic acid in seawater media, Deep Sea Research Part A. Oceanographic

465   Research Papers, 34(10), 1733-1743 1987.

466   Enriquez, R.M., Taylor, J.R: Numerical simulations of the competition between wind-driven

467   mixing and surface heating in triggering spring phytoplankton blooms. ICES J. Mar. Sci. J. du

468   Cons. fsv071, 2015.

469   Golbol, M., Vellucci, V., Antoine, D .: BOUSSOLE, https://doi.org/10.18142/1, 2000.

470   Hemming, M. P., Kaiser, J., Heywood, K. J., Bakker, D. C., Boutin, J., Shitashima, K., Onken,

471   R. : Measuring pH variability using an experimental sensor on an underwater glider. Ocean

472   Science, 13 , 427–442,2017.

473   Holte, J., & Talley, L. : A new algorithm for finding mixed layer depths with applications to

474   Argo data and Subantarctic Mode Water formation. Journal of Atmospheric and Oceanic

475   Technology, 26(9), 1920-1939, 2009.

476   Hood, E. M., and L. Merlivat .: Annual and interannual variations of fCO2 in the

477   northwestern Mediterranean Sea: Results from hourly measurements made by CARIOCA

478   buoys, 1995-1997, J Mar Res, 59, 113-131, 2001.

479   Lacour, L., Briggs, N., Claustre, H., Ardyna, M., & Dall'Olmo, G.: The intraseasonal

480   dynamics of the mixed layer pump in the subpolar North Atlantic Ocean: A

481   Biogeochemical‐Argo float approach. Global Biogeochemical Cycles, 33(3), 266–281,2019.

482   Lee, Z., Weidemann, A., Kindle, J., Arnone, R., Carder, K. L., & Davis, C. : Euphotic

483   zone depth: Its derivation and implication to ocean-color remote sensing. Journal of

484   Geophysical Research: Oceans , 112 (C3),2007.

485   Mahadevan, A., D'asaro, E., Lee, C., & Perry, M. J. : Eddy-driven stratification initiates

486   North Atlantic spring phytoplankton blooms. Science, 337(6090), 54-58, 2012.

487   Marty, J.-C., Chiavérini, J. .: Seasonal and interannual variations in phytoplankton

production at DYFAMED time-series station, northwestern Mediterranean Sea. Deep

Sea Res. Part II 49, 2017–2030, 2002.

Mehrbach, C., C. H. Culberson, J. E. Hawley, and R. M. Pytkowicx .: Measurement of the apparent dissociation constants of carbonic acid in seawater at atmospheric pressure, Limnol Oceanogr, 18(6), 897-907, 1973.

Merlivat, L., and Brault, P.: CARIOCA BUOY, Carbon Dioxide Monitor, Sea Technol., 23–30, 1995.

Merlivat, L., Boutin, J., & Antoine, D. : Roles of biological and physical processes in driving seasonal air–sea CO 2 flux in the Southern Ocean: New insights from CARIOCA pCO 2. Journal of Marine Systems, 147, 9-20, 2015.

Merlivat, L., Boutin, J., Antoine, D., Beaumont, L., Golbol, M., & Vellucci, V. : Increase of dissolved inorganic carbon and decrease of pH in near surface waters of the Mediterranean Sea during the past two decades. Biogeosciences, 15(18), 5653-5662, 2018.

Millot: Circulation in the Western Mediterranean Sea, Journal of Marine Systems, 20, 423–442, 1999.

Morel, A., and J. F. Berthon . : Surface pigments, algal biomass profiles, and potential production of the euphotic layer: relationships reinvestigated in review of remote-sensing applications, Limnol. Oceanogr., 34, 1545–1562, 1989.

Niewiadomska, Katarzyna, Claustre, Hervé, Prieur, Louis, d'Ortenzio, Fabrizio, (2008), Submesoscale physical‐biogeochemical coupling across the Ligurian current (northwestern Mediterranean) using a bio‐optical glider, Limnology and Oceanography, 53, doi: 10.4319/lo.2008.53.5_part_2.2210.

Papaioannou, G., Papanikolaou, N., and Retalis, D. : Relationships of photosynthetically active radiation and shortwave irradiance. Theoretical and Applied Climatology, 48: 23–27, 1993.

Pasqueron de Fommervault, O., Migon, C., D'Ortenzio, F., Ribera d'Alcalà, M., and Coppola, L.: Temporal variability of nutrient concentrations in the northwestern Mediterranean sea (DYFAMED time-series station), Deep-Sea Res. Pt. I, 100, 1–12, 2015.

516 Pellichero, V., Boutin, J., Claustre, H., Merlivat, L., Sallée, J.-B., & Blain, S. : Relaxation of

517 wind stress drives the abrupt onset of biological carbon uptake in the Kerguelen bloom: a

518 multisensor approach. Geophysical Research Letters, 47, e2019GL085992

519 https://doi.org/10.1029/2019GL085992, 2020.

520 Rödenbeck, C., Keeling, R. F., Bakker, D. C. E., Metzl, N., Olsen, A., Sabine, C., and

521 Heimann, M.: Global surface-ocean pCO2 and sea–air CO2 flux variability from an

522 observation- driven ocean mixed-layer scheme, Ocean Sci., 9, 193–216, doi:10.5194/os-9-

523 193-2013, 2013.

524 Rumyantseva, A, Henson, S, Martin,A , Thompson, A. F, Damerell G.M, Kaiser J, Heywood,

525 K.J.: Phytoplankton spring bloom initiation: The impact of atmospheric forcing and light in

526 the temperate North Atlantic Ocean, Progress in Oceanography, 2019.

527 Siegel, D. A., S. C. Doney, and J. A. Yoder (2002), The North Atlantic spring phytoplankton

528 bloom and Sverdrup's critical depth hypothesis, Science, 296, 730– 733.

529 Sverdrup, H. U.: On vernal blooming of phytoplankton. Conseil Exp. Mer, 18, 287-295,1953.

530 Takahashi, T., Sutherland, S. C., Wanninkhof, R., Sweeney, C., Feely, R. A., Chipman, D. W.,

531 Hales, B., Friederich, G., Chavez, F., Sabine, C., Watson, A., Bakker, D. C. E., Schuster, U.,

532 Metzl, N., Yoshikawa-Inoue, H., Ishii, M., Midorikawa, T., Nojiri, Y., Kortzinger, A.,

533 Steinhoff, T., Hoppema, M., Olafsson, J., Arnarson, T. S., Tillbrook, B., Johannessen, T.and

534 Olsen, A., Bellerby, R., Wong, C. S., Delille, B., Bates, N. R., and de Baar, H. J. W.:

535 Climatological mean and decadal change in surface ocean pCO2 and net sea-air CO2 flux

536 over the global oceans, Deep-Sea Res. II, 56, 554–577, 2009.

537 Taylor, J. R., & Ferrari, R.: Shutdown of turbulent convection as a new criterion for the onset

538 of spring phytoplankton blooms. Limnology and Oceanography, 56(6), 2293-2307, 2011.

539 Venables, H. and Moore, C.M.: Phytoplankton and light limitation in the Southern Ocean:

540 Learning from high nutrient, high chlorophyll areas. Journal of Geophysical Research:

541 Oceans, 115(C2), 2010.

542 Wanninkhof, R.: Relationship between wind speed and gas exchange over the ocean revisited.

543 Limnology and Oceanography: Methods, 12(6), 351–362, 2014.

544   Weiss, R.: Carbon dioxide in water and seawater: the solubility of a non-ideal gas, Marine
545   chemistry , 2 (3), 203–215, 1974

546

547

548   Figures and tables

549   Figure 1. The area of the northwestern Mediterranean Sea showing the French and Italian
550   Rivieras, the island of Corsica, the main current branches (green arrows) in the Ligurian Sea
551   and the location of the BOUSSOLE buoy (white square) and the AZUR meteorological buoy
552   (yellow square). The black line indicates the glider's path in March-April 2016.

553   Figure 2. 2016 (a) Hourly DIC (green) and SST (purple) at the BOUSSOLE site, (b) hourly
554   wind stress (blue) and net heat flux (pink) at the Azur buoy site. The pink dotted line indicates
555   the change of sign of the net heat flux from negative to positive values, (c) daily depths of the
556   mixed layer (black), mixing layer (dotted black), Ekman layer (cyan) and euphotic layer
557   (orange) at the BOUSSOLE site. The black dotted line on panels (a), (b), (c) (d) and (e)
558   indicates the onset time of the bloom (18 March). (d) PAR (orange) and average mixing layer
559   irradiance (blue), (e) Glider-derived depths of the mixed layer (black curve, same as in (c)),
560   euphotic layer (orange), and nighttime 2-day binned chlorophyll concentration (green
561   coloring) retrieved between March 7 and April 5.

562   Figure 3. (a, b, c) 2017, 2018 and 2019 DIC (green) and SST (purple) at the BOUSSOLE site,
563   (d, e, f) wind stress (blue) and net heat flux (red) at the Azur buoy site. The red dotted line
564   indicates the change of sign of the net heat flux from negative to positive values, (g, h, i)
565   depths of the mixing layer (dotted black), Ekman layer (cyan) and euphotic layer (orange) at
566   the BOUSSOLE site. The vertical dotted green line indicates the onset of the bloom.

567   Figure 4. Changes of physical parameters (hourly values) at the onset of the 2016 bloom
568   during 2 consecutive periods of 4 days, March 14-17 (blue) and March 18-21 (red) as a
569   function of wind stress (a) net surface heat flux (b) depths of the Ekman, mixing and euphotic
570   layer. Grey circles and grey squares indicate mean values respectively on March 17 and
571   March 18. For comparison, the orange line shows the euphotic layer depth (March 14-21).

572   Figure 5. From March 7 to April 5, (a) DIC and Chla. The purple line and the squares
573   (blue,morning; grey, evening) indicate the 3 days biological diurnal DIC changes during the

574 period considered to compute NCP The blue and orange lines indicate the surface Chla when
575 the glider was at a distance of less than 5 km (blue) and less than 20 km (orange) respectively
576 from the BOUSSOLE buoy. (b) PAR and I average mixing layer irradiance. The vertical
577 dotted black line indicates the onset of the bloom on March 18.

578 Table 1. Net community production computed in the mixing layer over 3 days (NCP) after the
579 bloom onset (T_0). (a, b) variation of DIC at the measurement depth and linked correlation
580 coefficient; (c, d) change of integrated DIC over Z_{mx} and linked correlation coefficient ;(e)
581 CO_2 flux from the atmosphere to the ocean; (f), absolute value of calculated NCP is
582 considered in order to provide positive values throughout the presentation and discussion in
583 the manuscript.

584 Table 2. 2016-2019. Atmospheric drivers of the onset of the bloom: average values and
585 standard deviation on the day of the start of the bloom, T_0.

586